parameters changed during the analysis following the hardening of the concrete. With this analysis the optimum demoulding time can be estimated as well. To the demoulding load a lifting and tearing force was added to the early age concrete slab. After this, but also in early ages, a rotation effect occurs: the demoulding was made upside down, but the racking of the precast slabs were in the other direction. In this two load case the lifting and rotating of the elements were also checked. The next situation was the storing load case. In this case the weight of three elements were added to the slab, simulating the effect of the stacking. The highlighted design target was to check the ultimate and serviceability limit states under the train's load and thus the geometry of the trains were added. To examine the worst loading case, and to model the passage of the train, seven different loading scenarios were carried out in different positions. In the Ultimate Limit State (ULS) the principal stresses were checked and in the Serviceability Limit State (SLS) the crack widths and the vertical displacements were checked. During the calculation the unequal rail loading was also taken into consideration. To be able to calculate the effect of the cyclic loading fatigue analysis was done also for all the loading positions. The number of the cycles were calculated back from the estimated lifetime of the structure and the average daily traffic, and it leads to 20 000 000 cycles. The finite element software calculated two additional fatigue strains for the maximum fracturing strain (Pryl et al. 2010), one handled the tensile strength reduction during the cyclic load (according to the Wöhler curve), and the other takes into consideration the crack opening effect during the cyclic load.

The structure complied with all the design requirements both in ULS and in SLS. In ULS the target was that the structure resists the loads with the appropriate safety factors and with design material parameter values without the failure of the structure. In SLS the aim was that the crack widths should be less than the value according to Eurocode 2 (0.2 mm). Both design cases met the requirements in every loading position and design situation. The slabs deformation followed the expectation under the different loads. The connection between the two slabs worked well. It also can be seen that the structure is highly optimized. In ULS several cracks appeared in the surface of the structure, but without failure, and in SLS almost no visible cracks appeared in the structure.

3.3 Real scale test

The PCAT slab was installed within their test pit to measure the actual deflection of the slab along the structure using an applied load at various locations. The position of the load was replicated the arrangement used in the FEM simulation. The PCAT off-street slab was designed for 12 tonne axle loads. For the testing it was proposed, after the first suite of loading at 8 tonne that the load be increased in 4 tonne increments up to 24 tonne, subject to slab performance during the test. It was a static test, no cyclic loading was applied to the structure in this phase of testing. Table 1 shows the concrete mix design used for the slabs.

1. Table: Concrete mix design

Materials	Batch Weight [kg/m^3]
Aggregate 1: 4/10mm limestone	802
Aggregate 2: 0/4mm Sand	842
Limestone Powder	130
Cement: Cem I Class 52.5N	400
Fibres: synthetic fibres	5.0
Admixture: Superplasticizer	3.0

The loading of the slab was carried out using the Rail Trackform Stiffness Tester (RTST) (Figure 6) which was been developed by AECOM to replicate the loading requirements of high-speed or heavy-haul lines through the use of an increased range of pulse-loading conditions. The RTST apparatus is mounted on a transport frame that can be moved along on rubber-caterpillar tracks whilst off track and then switched to rail wheels. On ballasted track geophones measure the deflection response of the ballast, sub-ballast, formation and subgrade enabling assessment of layer stiffness. During testing of the PCAT slab an array of 9 geophones were positioned above the concrete slab surface to record the deflection in microns.

To ensure the previously presented numerical model's property, a finite element analysis was calculated for the RTST test. The model contained the whole test setup including: the concrete pit, the compacted soil, and the two slabs with the previously mentioned detail. The effect of the RTST was added to the slab with using a steel plate which corresponds to the loading beam's foot. The measured value in the finite element model was the vertical deflection. It was measured at 9 different points replicating where the geophones were positioned for the actual test. The position of the loading plate in the finite element model followed the RTST machines position in the test. The measuring points were according to Figure 6.

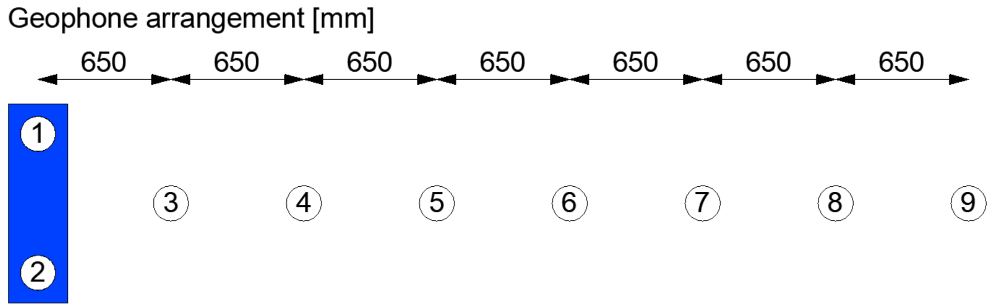

Figure 6: The measuring points of RTST testing (AECOM PCAT Test report)

The results in every loading case were close to each other. The finite element analysis closely mirrored what happened in reality and the differences between the measured deflections in the model and in the test was less than 0.1 mm. Only one loading scenario was where the difference was higher than modelled and this was where the load was positioned over the female joint. This was outlined in the AECOM report which determined a very poor subgrade stiffness in this area. The results of the test and the FEA can be seen in Figure 7.

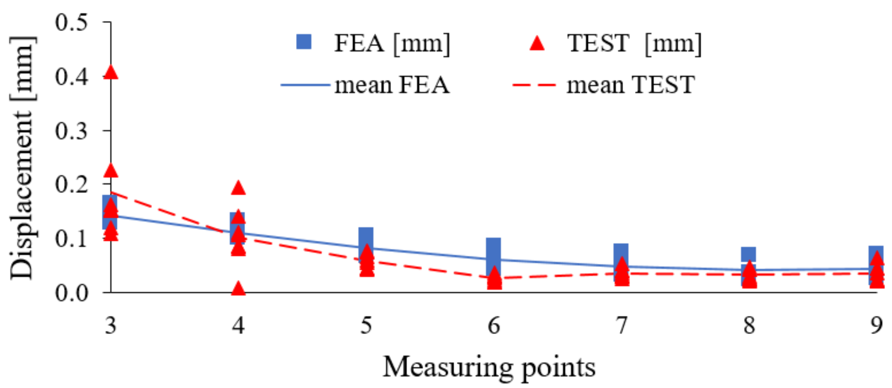

Figure 7: Results of RTST and FEA

4 Summary

The use of macro synthetic fibre reinforced concrete has become more and more popular in the building industry and thus also in the concrete track slab constructions. Track slab structures are typically heavily exposed to weather and mechanical loads, and because of this must have sufficient ductility and durability. At the same time the repair or replacement of these elements is difficult as generally the traffic must be stopped for a long periods during this process. Based on these criteria the use of macro synthetic fibre is a good alternative reinforcement to mesh and steel bars. The concrete reinforced with the already mixed in corrosion-free fibres is easy to handle and the track slab can be constructed faster, thus by using FRC, labour can be decreased and the ductility increased. Further macro synthetic fibres are better for dynamic loads also, which is a significant advantage of this type of construction.

Design and optimizing of the track slab means the determining of the required thickness of the track slab and the macro synthetic fibre dosage for the varying load cases, such as ultimate and serviceability limit state, and fatigue. For these special tasks advanced finite element software is needed. The influence of the fibres could be taken into account by the modification of the fracture energy of the plain concrete. These design models have been validated by full scale laboratory tests.

5 References

Cervenka, J., Papanikolaou, V. K. (2008), *Three dimensional combined fracture-plastic material model for concrete*, International Journal of Plasticity (24) pp. 2192-2220.

EUROCODE EN 1992 (2004), *European Code for design of concrete structures: European Committee for Standardization*, Brussels.

Hammond, J. (2016), *Construction and Reinforcement*, Railing Professional October 2016 Issue, pp. 162-163.

ITAtech Activity Group Support 2015, (2015), *ITAtech Design Guidance For Precast Fibre Reinforced Concrete Segments*, ITAtech Report n7, draft.

Juhász K. P. (2013), *Modified fracture energy method for fibre reinforced concrete*, Fibre Concrete 2013: Technology, Design, Application, pp. 89-90.

Kolmar, W. (1986), *Beschreibung der Kraftuebertragung über Risse in nichtlinearen Finite-Element-Berechnungen von Stahlbetontragwerken*, Dissertation, T.H. Darmstadt.

Menétrey, P., William, K. J. (1995), *Triaxial Failure Criterion for Concrete and Its Generalization*, ACI Structural Journal, 92(3), pp. 311-318.

Nagy J., Juhász K. P., Mészáros A. (2014), *The beginning: the tramway in Szeged*, Innoteka, 2014 September, pp. 24-25.

Nagy J., Juhász K. P., Herman S., Herman K. (2015a), *Az első magyar, műanyag szállal erősített és füvesített villamospálya 1. rész (The first Hungarian synthetic fibre reinforced and grassed tramline 1st part)*, Sínek világa, 2015/2, pp. 18-21.

Nagy J., Juhász K. P., Herman S., Herman K. (2015b), *Az első magyar, műanyag szállal erősített és füvesített villamospálya 2. rész (The first Hungarian synthetic fibre reinforced and grassed tramline 2nd part)*, Sínek világa, 2015/3, pp. 10-14.

Ridout, A. (2009), *Macro-fibre-reinforced concrete slab track*, Concrete, September 2009, pp. 16-18.

Vandewalle, L., et al. (2002), *RILEM TC 162-TDF : Test and design methods for steel fibre reinforced concrete,* Materials and Structures, Vol. 33, January-February 2000, pp 3-5.

Closed-form Solutions for Interaction Diagrams of Hybrid Fiber-Reinforced Tunnel Segments

Yiming Yao[1], Mehdi Bakhshi[2], Verya Nasri[2], Barzin Mobasher[3]

[1] : Key Laboratory of Concrete and Prestressed Concrete Structures of Ministry of Education, School of Civil Engineering, Southeast University, Nanjing, China.

[2] : AECOM, New York, United States.

[3] : Arizona State University, Tempe, United States.

Abstract

Precast concrete segments are the predominant support method used in tunnels dug by Tunnel Boring Machines (TBM) in soft ground and weak fractured rock, providing the initial and final ground support. Conventionally, steel bars are used in concrete segments to resist tensile stresses due to all loading cases from the time of casting through service condition. With traditional reinforcement, a significant amount of time and labor are needed to assemble the cages and place the reinforcing bars. Fiber reinforced concrete (FRC) has become more attractive for its use in tunnel lining construction as a result of improved post-cracking performance, crack control characteristics and capability of partial replacement of steel bars. Due to the strength requirements in large-diameter tunnels, which are subjected to embedment loads and TBM thrust jack forces, the use of FRC is not adequate as the sole reinforcing mechanism. Therefore, the hybrid fiber-reinforced concrete (HRC) combining both rebars and steel fibers is frequently used in practice. Tunnel segmental linings are designed for load cases that occur during manufacturing, transportation, installation, and service conditions. With the exception of two load cases of TBM thrust jack forces and longitudinal joint bursting load, segments are subjected to combined axial force and bending moment. Therefore, P-M interaction diagrams have been used as the main design tool for tunnel engineers.

Standard FRC constitutive laws recently allow for a significant residual strength in tension zone below the neutral axis. However, design capacity of HRC segment is significantly underestimated using conventional Whitney's rectangular stress block method, especially for tension-controlled failure, since the contribution of fibers in tension zone is ignored. Methods that currently incorporate contribution of fibers on P-M diagrams are based on numerical and finite-element analyses, which are normally more complicated and not readily to be implemented for practical design tools. Closed-form solutions of full-range P-M interaction diagram considering both rebar and fiber contributions are presented in this paper for HRC segments. The proposed model is verified with experimental data of compression tests with eccentricity as well as other numerical models for various cases of HRC sections. Results show that using appropriate material models for fiber and reinforcing bar, engineers can use the proposed methodology to obtain P-M interaction diagrams for HRC tunnel segments.

Keywords

Analytical method; fiber; hybrid fiber-reinforced concrete; interaction diagram; tunnel, lining; residual strength; segment; TBM

https://doi.org/10.35789/fib.BULL.0095.Ch18

1 Introduction

Precast concrete segments reinforced with steel bars are the predominant support method used in tunnels dug by Tunnel Boring Machines (TBM), where a significant amount of time and labor are needed to assemble the cages and place the reinforcing bars (Bakhshi and Nasri 2014a; b). Alternatively, fibers may considerably improve the concrete post-cracking behavior, and allow for better crack control and shrinkage, fatigue and impact resistance (Bakhshi and Nasri 2015; Briffaut et al. 2016). In addition, fibers may enhance handling and placement of precast concrete segments by reducing job-site labor requirements. Furthermore, uniform dispersion of fibers throughout the segment guarantees the presence of the reinforcement action in areas around the segment face, where bursting and spalling stresses develop during the TBM jacking process (Bakhshi and Nasri 2014c; d). The use of FRC is sometimes not adequate as the sole reinforcing material, especially for large diameter tunnels. Therefore, a hybrid solution of combined rebar and fiber reinforcement has been adopted (Plizzari 2009; Tiberti et al. 2015). In shallow large-diameter tunnel segments, low internal axial forces and high bending moments as well as high TBM thrust forces are present. Such loading conditions impose high localized flexural, bursting and spalling stresses that can be better resisted by reinforcing bars than fibers (Tiberti 2009). Also, in large-diameter tunnels with an increased ratio between the tunnel diameter and lining thickness, segments are more likely to withstand the high flexural stresses due to imperfections and irregular construction (Tiberti 2009).

Tunnel segmental linings are mainly subjected to combined axial force and bending moment due to multiple loading cases that occur during manufacturing, transportation, installation, and service conditions (ACI 544 2016). Axial force-bending moment interaction (P-M) diagram is therefore an important tool that tunnel engineers use for the structural design. This diagram, originally presented by Whitney and Cohen (1956), continues to be widely used today (Hernandez-Montes et al. 2005) and has been investigated extensively by numerous researchers (Bresler 1960; Parme et al. 1966; Rotter 1985). However, most of the work carried out using the Whitney's rectangular stress block only considers concrete strength in compression zone, which significantly underestimated the design capacity of FRC or hybrid fiber-reinforced concrete (HRC) tunnel segments. ACI 544.7R (ACI 544 2016) presents a simplified method for derivation of the P-M interaction diagram for precast concrete segments reinforced solely by fibers. However, the method cannot be extended to HRC segments using a superposition approach as steel material model was not considered. Methods that incorporate contribution of fibers and steel rebar in the tensile zone of cross section are based on numerical and finite-element analyses to construct the P-M interaction diagrams of HRC sections (Chiaia et al. 2007, 2009; de la Fuente et al. 2012; Tiberti 2009). Despite of popularity and abundance of numerical methods, closed-form solutions offer important advantages for engineering problems including computational efficiency, readily parametric studies, and easy to be implemented into a simple and user-friendly spreadsheet program. Mobasher et al. (2015) derived closed-form solutions for analysis of flexural load-deflection of HRC beams subjected to pure bending. Although, this methodology has been proved robust in design of HRC elements subjected to pure bending, the model needs to be significantly modified so that the effects of axial forces on flexural capacity can be fully captured.

This paper presents material models, derivations and for the first time, closed-form solutions to construct a full range P–M interaction diagram of HRC segments considering the contributions of fibers in the post-cracking strength in addition to reinforcing bars. The proposed methodology covers all the failure modes in the tunnel precast segments subjected to the combined axial forces and bending moments. Parametric studies for key design parameters are presented. The model is verified by simulating experimental results from published data for HRC columns and several other model-predicted and numerical results for HRC precast segmental and cast-in place concrete tunnel linings. A spreadsheet based program has also been developed and available for general users to readily construct the interaction diagram with the present method. The proposed P–M diagram based on the associated program can be used as a tool for design of HRC tunnel segments especially in large diameter tunnels.

2 Model Derivations

2.1 Multi-linear stress-strain models

The objective of this study is to develop the analytical closed-form solutions of the P-M interaction diagram of the HRC section. Fig. 1 presents three distinct material models used in the derivation of parametric response of HRC beams addressing concrete and steel's tensile and compressive piecewise linear constitutive laws. Note that material variables are normalized with respect to tensile modulus E and the first cracking tensile strain ε_{cr}. Fig. 1(a) shows the tension model with an elastic tensile stress with modulus E increasing up to the first cracking tensile strength of coordinates (ε_{cr}, σ_{cr}). In the post-crack region, the tensile stress is constant at $\sigma_p = \mu\sigma_{cr} = \mu\varepsilon_{cr}E$ and terminates at the ultimate tensile strain $\varepsilon_{tu} = \beta_{tu}\varepsilon_{cr}$. The simplified bilinear tension model is capable of covering a wide range of tension softening behavior exhibiting both deflection-hardening and deflection-softening responses in flexure (Soranakom and Mobasher 2007). Strain hardening behavior, which normally requires high steel fiber dosages (1-2% by volumetric fraction or a dosage of 77-154 kg/m^3), can be also captured by extending the proposed tension model and including a hardening branch (Yao 2016). Fig. 1(b) shows the elastic-perfectly plastic compression response with a modulus $E_c = \gamma E$. The plastic range initiates at strain $\varepsilon_{cy} = \omega\varepsilon_{cr}$ corresponding to yield stress $\sigma_{cy} = \omega\gamma\varepsilon_{cr}E$ and terminated at $\varepsilon_{cu} = \lambda_{cu}\varepsilon_{cr}$. The effect of lateral ties on the compressive behavior is characterized by an improved compressive strength $\sigma_{cy,c} = \omega_c\gamma\varepsilon_{cr}E$ and ultimate strain $\varepsilon_{cu,c} = \lambda_{cu,c}\varepsilon_{cr}$. Fig. 1(c) is the elastic-perfectly plastic steel model using yield strain and stress of $\varepsilon_{sy} = \kappa\varepsilon_{cr}$ and $f_{sy} = \kappa n\varepsilon_{cr}E$. Stress-strain curve of steel is terminated at the specified strain limits defined by the design codes discussed in the following sections. Fig. 1(d) shows the steel parameters defined as area $A_s = \rho_g bh$ at the reinforced depth αh for both compression and tension rebar. The compression reinforcement ratio, ρ_g', is assumed equal to the tension reinforcement ratio, ρ_g, throughout this study.

The material models for tension and compression of FRC and steel rebar are presented as:

$$\sigma_t(\varepsilon_t) = \begin{cases} E\varepsilon_t & 0 \le \varepsilon_t \le \varepsilon_{cr} \\ \mu E\varepsilon_{cr} & \varepsilon_{cr} < \varepsilon_t \le \varepsilon_{tu} \\ 0 & \varepsilon_t > \varepsilon_{tu} \end{cases} \quad ; \quad \frac{\sigma_t(\beta)}{E\varepsilon_{cr}} = \begin{cases} \beta & 0 \le \beta \le 1 \\ \mu & 1 < \beta \le \beta_{tu} \\ 0 & \beta > \beta_{tu} \end{cases} \tag{1}$$

$$\begin{aligned}
&\textit{unconfied}:\\
&\sigma_c(\varepsilon_c)=\begin{cases}E_c\varepsilon_c & 0\le\varepsilon_c\le\varepsilon_{cy}\\ E_c\varepsilon_{cy} & \varepsilon_{cy}<\varepsilon_c\le\varepsilon_{cu}\\ 0 & \varepsilon_c>\varepsilon_{cu}\end{cases};\qquad \frac{\sigma_c(\lambda)}{E\varepsilon_{cr}}=\begin{cases}\gamma\lambda & 0\le\lambda\le\omega\\ \gamma\omega & \omega<\lambda\le\lambda_{cu}\\ 0 & \lambda>\lambda_{cu}\end{cases}\\
&\textit{confined}:\\
&\sigma_{c,c}(\varepsilon_c)=\begin{cases}E_c\varepsilon_c & 0\le\varepsilon_c\le\varepsilon_{cy,c}\\ E_c\varepsilon_{cy,c} & \varepsilon_{cy,c}<\varepsilon_c\le\varepsilon_{cu,c}\\ 0 & \varepsilon_c>\varepsilon_{cu,c}\end{cases};\qquad \frac{\sigma_{c,c}(\lambda)}{E\varepsilon_{cr}}=\begin{cases}\gamma\lambda & 0\le\lambda\le\omega_c\\ \gamma\omega_c & \omega_c<\lambda\le\lambda_{cu,c}\\ 0 & \lambda>\lambda_{cu,c}\end{cases}
\end{aligned}\tag{2}$$

$$f_s(\varepsilon_s)=\begin{cases}E_s\varepsilon_s & 0\le\varepsilon_s\le\varepsilon_{sy}\\ E_s\varepsilon_{sy} & \varepsilon_s>\varepsilon_{sy}\end{cases}\quad;\quad \frac{f_s(\chi)}{E\varepsilon_{cr}}=\begin{cases}n\chi & 0\le\chi\le\kappa\\ n\kappa & \chi>\kappa\end{cases}\tag{3}$$

where normalized independent variables for strains are defined as $\beta=\varepsilon_t/\varepsilon_{cr}$, $\lambda=\varepsilon_c/\varepsilon_{cr}$ and $\chi=\varepsilon_s/\varepsilon_{cr}$.

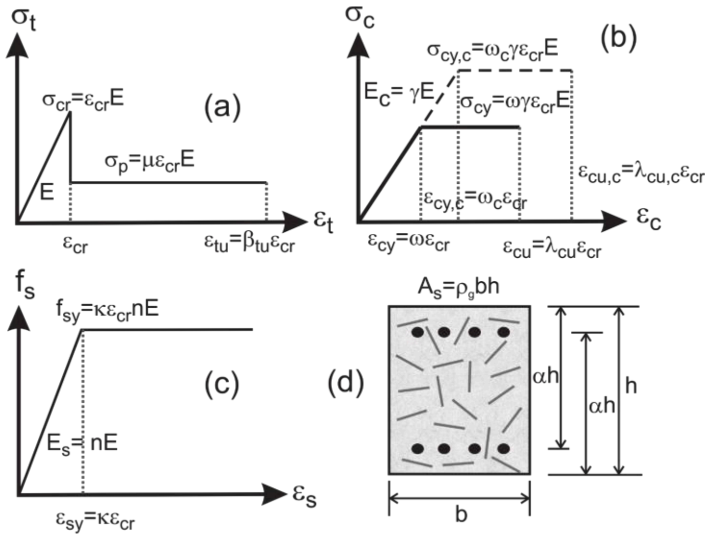

Fig. 1: *Material models including (a) FRC tensile model, (b) FRC compressive model, (c) steel model, (d) cross section.*

Demands of sufficient ductility of members under compression and bending actions require the use of lateral confinement, which results in a modification of the effective stress-strain relationship in compression. Since the present model is developed based on normalized parameters, the improved strength and strain limits due to confinement can be directly assigned according to the specific design considerations and available experimental data. A numerical example was given by authors (Yao et al. 2018) to incorporate fib Model Code equations into lateral confinement effects on compressive strength and ultimate strain.

2.2 Derivation of axial force and bending moment

In derivation of axial force (P) and bending moment (M) for a rectangular cross section, the assumption of plane section remaining plane is used. Axial and flexural deformations are incrementally imposed by taking the normalized strain at the bottom extreme fiber β as the independent variable (λ represents the strain at the top extreme fiber). In this study, the compressive strain is defined as positive, and the stress and force terms follow the same sign convention. The stress distributions are obtained by applying linear strain distribution across the depth using the material models mentioned in section 2.1. Different modes of failure including all compression, compression-controlled and tension-controlled are determined depending on the strain at bottom extreme fiber and strain of steel.

The stress distributions of different modes of failure are shown in Fig. 2. The Mode 1 corresponds to range where the entire cross section is under compression, with two sub-modes: 1.1 extreme compression fiber exceeds yield strain in compression ($\lambda \geq \omega$), 1.2 extreme compression fiber does not exceed yield strain in compression ($0 < \lambda < \omega$); Mode 2 corresponds to compression controlled failure where the steel in tensile region has not yielded ($-\kappa \leq \chi \leq 0$), which also includes two sub-modes: 2.1 no tension crack ($-1 \leq \beta \leq 0$) and 2.2 tension crack ($\beta<-1$). Finally, Mode 3 corresponds to the tension controlled failure ($-0.005/\varepsilon_{cr} < \chi \leq -\kappa$) with two scenarios existing in each sub-stage: 3.1 when the compression steel is elastic or 3.2 when the compression steel is yielding. Under modes 2 and 3, where the bottom extreme fiber is in tension ($\beta < 0$), a parameter k is introduced to represent the normalized height of natural axis:

$$kh = h_{c1} + h_{c2}$$
$$\frac{\lambda_{cu}\varepsilon_{cr}}{kh} = \frac{-\beta\varepsilon_{cr}}{h-kh} \quad or \quad \beta = -\frac{1-k}{k}\lambda_{cu} \tag{4}$$

The stresses are then integrated over the area in each zone to obtain the parametric solutions of force terms, and the solution for the depth of neutral axis can be obtained analytically. Internal moment is obtained by integrating the force components using the distance to the center line as the moment arm. Normalized force and moment in different modes are presented in Table 1, where the force (P_i) and moment (M_i) are normalized with respect to the values P_{cr} and M_{cr} at tensile cracking:

$$P_i = P_i{'}P_{cr}; \qquad P_{cr} = bhE\varepsilon_{cr} \tag{5}$$

$$M_i = M_i{'}M_{cr}; \qquad M_{cr} = \frac{1}{6}bh^2E\varepsilon_{cr} \tag{6}$$

Strain limits of the materials are required by design codes to ensure sufficient ductility of structural members. Ultimate compressive strain of concrete and ultimate tensile elongation of reinforcing steel are normally specified as the ductility limits of RC sections. For example, ACI 318-14 (2014) and CSA 23.3-14 (CSA 2014) specify a maximum concrete compressive strain of 0.003 for normal strength concrete (NSC) and at least 14% elongation for ductile steel. fib Model Code 2010 (2013) uses a maximum strain of 0.0035 for NSC with characteristic strength up to 50 MPa which reduces to 0.0028 for high strength concrete (HSC) up to 90 MPa. Four ductility classes were defined for reinforcing steel with characteristic elongation at maximum force up to 8%. The present model is derived based on two ultimate variables for ultimate strain in the extreme compression fiber of ε_{cu}, and ultimate tensile strain of β_{tu}. The desired strain limits can be assigned to the model parameters to accommodate the design codes of different countries as well as materials strength, classes and confinement conditions.

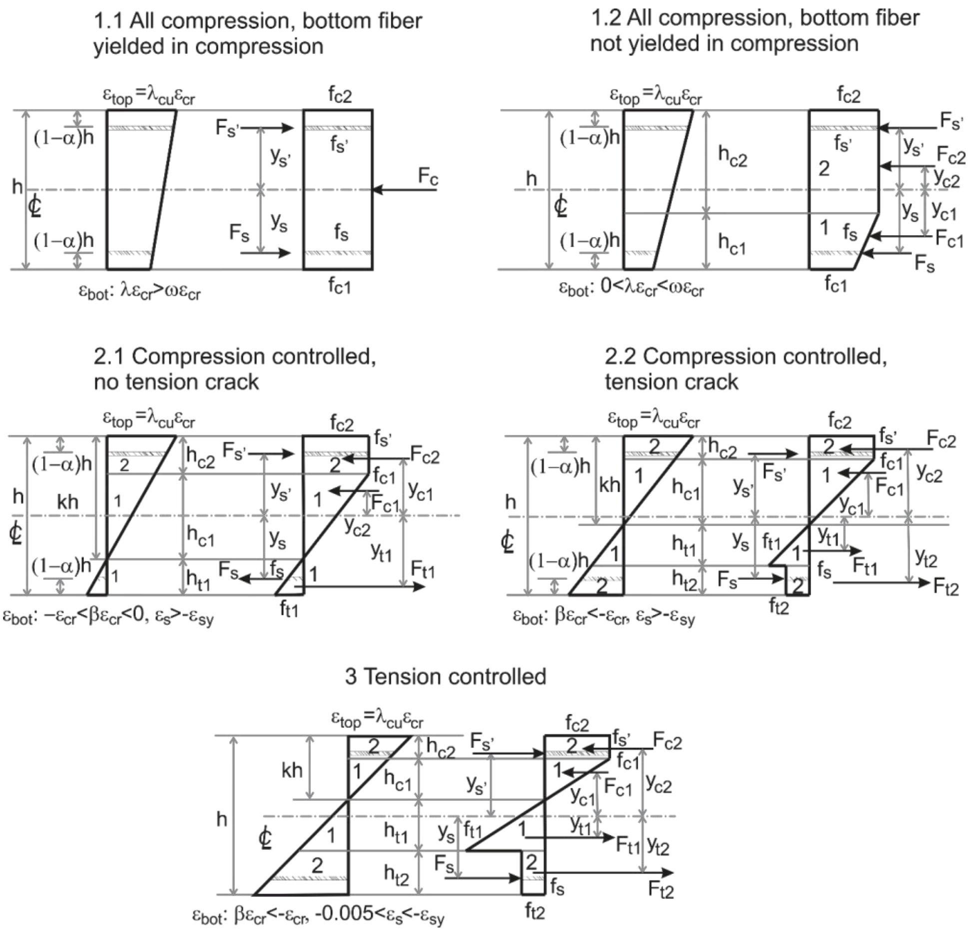

Fig. 2: *Strain and stress diagrams at different failure modes including 1.1 all compression with bottom fiber yielded in compression, 1.2 all compression while bottom fiber is not yielded, 2.1 compression controlled, no tension crack, 2.2 compression controlled with crack in tension, 3 tension controlled.*

Using the derivations for axial force and bending moment under different cases, one can generate P-M interaction diagram based on intersections of two competing modes and the shorter length of the P-M Vector. A MATLAB code and an interactive spreadsheet were developed to implement the analytical expressions. A base numerical model for normal strength HRC is used to illustrate the modelling procedure with material properties: σ_{cy} = 40 MPa, E = 30 GPa, ε_{cr} =110(10)$^{-6}$, ε_{cu} = 0.0035, σ_p = 1.1 MPa, E_s = 210 GPa, f_{sy} = 500 MPa, ρ_g = 0.25%, steel elongation to failure of 12%, and reinforcement depth ratio 0.9. The normalization of parameters results in : μ =*0.33*, β_{tu} = 2000, γ = 1.0, ω = 12, λ_{cu} = 32, n = 7, κ = 19, and α = 0.9. Note that the full range interaction diagram can be obtained at much lower steel strain values compared to the elongation to failure, so the maximum β attained in this case was 776. The normalized interaction diagram is shown in Fig. 3, with all the modes of potential failure identified.

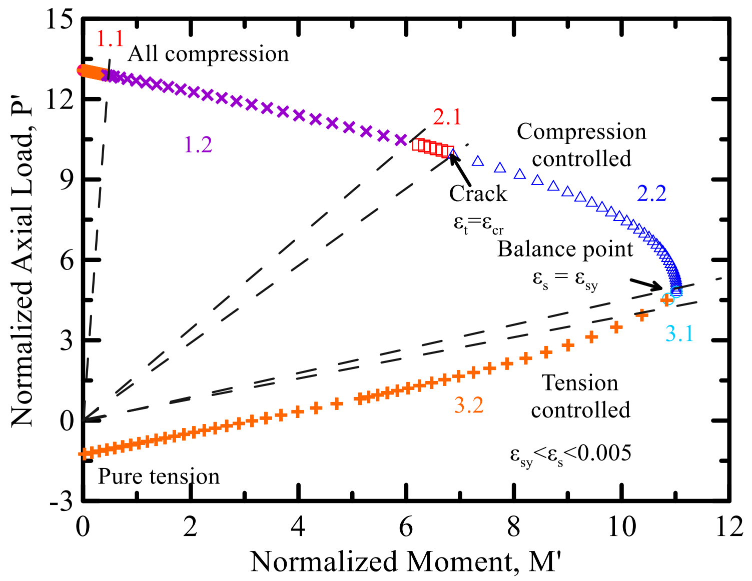

Fig. 3: *Normalized P-M diagram showing different failure modes.*

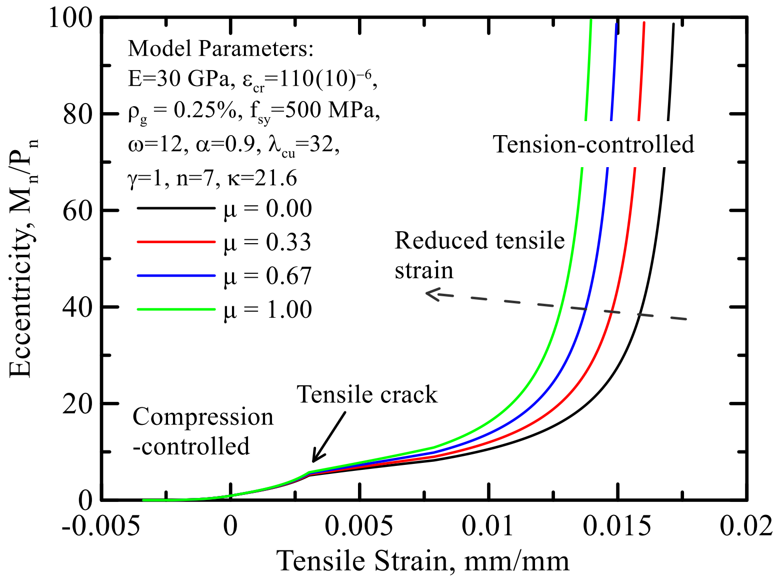

Fig. 4: *Normalized P-M diagram showing different failure modes including 1.1 all compression*

Besides the interaction diagram, the force and/or moment responses at limit states can also be correlated with the ductility parameters such as the strain and curvature. Serviceability based design limits can be readily identified and the effects of main parameters can also be revealed. Fig. 4 illustrates the variations of tensile strain at the extreme fiber with the eccentricity e (M_n/P_n), where the effects of μ are investigated. Two stages of low and high eccentricities are identified in the curves. The behavior in the first stage is dominated by compressive action when steel fibers have not played a role yet. As bending moment increases and the first tensile crack occurs, the behavior gradually turns into flexural action and the mode of failure is dominated by tension. In this stage, the effects of fiber bridging are more pronounced in improving the moment capacity and reducing the deformation at same loading level. As Fig. 4 shows, considerable reduction in tensile strain is observed with